Large Tunable Perpendicular Magnetic Anisotropy in $Y_{3-x}Tm_xFe_5O_{12}$ ($x = 0$–3) Epitaxial Films with Minor Changes in Switching Current

He Bai,[1,2,3] Z.Z. Zhu,[1] J.T. Ke,[1,4] Gang Li,[1] Jian Su,[1] Ying Zhang,[1] Tao Zhu,[1,3] and J.W. Cai[1,4,*]

[1] *Beijing National Laboratory for Condensed Matter Physics, Institute of Physics, Chinese Academy of Sciences, Beijing 100190, China*

[2] *Institute of High Energy Physics, Chinese Academy of Sciences, Beijing 100049, China*

[3] *Spallation Neutron Source Science Center, Dongguan 523803, China*

[4] *School of Physical Sciences, University of Chinese Academy of Sciences, Beijing 100049, China*

(Received 18 October 2021; revised 15 January 2022; accepted 28 April 2022; published 10 June 2022)

We show perpendicular magnetic anisotropy (PMA) in substituted rare-earth iron garnet $Y_{3-x}Tm_xFe_5O_{12}$ ($x = 0$–3) films epitaxially grown on (111) $(Gd_{0.63}Y_{2.37})(Sc_2Ga_3)O_{12}$ substrates by magnetron sputtering. With Tm concentrations varying from $x = 0$ to $x = 3$, the effective PMA field of the 10-nm-thick films increases monotonically from 0.3 to 2.7 kOe together with a similar coercivity increase from 2 to 65 Oe. The substituted garnet films with x ranging from 0.6 to 1.2 are structurally much more robust against epitaxial strain relaxation. Magnetotransport measurements in the $Y_{3-x}Tm_xFe_5O_{12}$/Pt heterostructure show that the anomalous Hall effect and spin Seebeck effect are significant and change little with Tm concentration, indicating that the interface spin-exchange interaction and interface spin-current transmission mainly depend on the net moment of Fe^{3+} sublattices rather than the total moment of $Y_{3-x}Tm_xFe_5O_{12}$. Importantly, the critical current density for the spin-orbit-torque-induced switching also changes very little with a minor increase from 1.76×10^{11} to 1.83×10^{11} A m^{-2}. We tentatively attribute this weak PMA-dependent current density to modification of the domain-wall depinning by the current. Our results demonstrate that substituted rare-earth iron garnets can be a general approach to tune PMA within a large range with nearly constant switching current, and yet there is plenty of work left to be done for more efficient SOT-based garnet ferrimagnet spintronics devices.

DOI: 10.1103/PhysRevApplied.17.064023

I. INTRODUCTION

Rare-earth iron garnets (REIGs), especially $Y_3Fe_5O_{12}$ (YIG), were extensively studied for microwave devices [1,2] and magneto-optical applications [3,4]. In recent years, these insulating ferrimagnetic films with unique properties, such as long spin-transmission length, low damping, and free from Joule heat, have continuously attracted a great deal of attention in spintronics. However, with very low magnetocrystalline anisotropy and small magnetostriction constants, thin YIG films (as well as many other REIG films) usually favor in-plane spontaneous magnetization due to the overwhelming shape anisotropy. It is important to fabricate REIG films with perpendicular magnetic anisotropy (PMA). Such perpendicularly magnetized insulating films, with their magnetization manipulated by spin-orbit torque (SOT), offer the potential for energy-efficient magnetic memory and logic devices [5,6] and optospintronics applications [7].

Historically, perpendicular magnetization was realized in micrometer-thick REIG films prepared by the liquid-phase-epitaxy (LPE) technique via growth-induced pair anisotropy [8]. By utilizing the different thermal expansion coefficients between quartz and YIG, thermal-strain-induced PMA was reported in very thick YIG films on quartz substrates fabricated by the vapor-deposition technique [9]. Currently, there is a common way to achieve PMA in nanometer-thick REIG films of high quality by promoting magnetoelastic anisotropy to overcome the shape anisotropy, specifically through epitaxial-lattice-strain manipulation. In fact, taking into account magnetostriction constants and lattice mismatch between REIGs and various garnet substrates, together with growth parameters, quite a few kinds of thin single-crystalline films with different saturation magnetization (M_s) fabricated by either pulsed laser deposition (PLD) or magnetron sputtering exhibit perpendicular spontaneous magnetization. These films include $Tm_3Fe_5O_{12}$ (TmIG) [10,11]; $Sm_3Fe_5O_{12}$ (SmIG) [12]; $Tb_3Fe_5O_{12}$ (TbIG) [13]; $Eu_3Fe_5O_{12}$ (EuIG) [14]; Mn-, Ce-, and Bi-substituted YIG [15–17]; and even pure YIG [18,19] with different PMA constants (K_u). It

*jwcai@aphy.iphy.ac.cn

should be mentioned parenthetically that, since linear magnetostriction originates from spin-orbit coupling, the different magnetostriction constants for REIGs are primarily due to different spin-orbit coupling for the corresponding rare-earth ions. From the past achievements in thin REIG films, one may expect to tune the K_u value over a large range simply by changing the ratio of different rare-earth ions.

On the other hand, SOT-induced magnetization switching is demonstrated in TmIG/Pt, YIG/Pt, and TbIG/Pt heterostructures with PMA, but the values of the threshold switching current density (j_c) are rather scattered. The results do not show any correlation between j_c and the effective PMA field ($H_K = 2K_u/M_s - 4\pi M_s$) or the rare-earth-ion type of REIGs. For the TmIG(8 nm)/Pt(5 nm) bilayer with $H_K \approx 2.7$ kOe, j_c is about 1.8×10^{11} A m^{-2} with an in-plane field (H_x) of 500 Oe along the current direction [5]. Later, a similar j_c was reported with H_x reduced to 2 Oe in TmIG(9.6 nm)/Pt(4 nm) with $H_K = 0.7$ kOe [20]. For the YIG(5 nm)/Pt(3 nm) bilayer with a smaller H_K of 0.5 kOe, j_c is as large as 3.0×10^{11} A m^{-2} with an in-plane field of 50 Oe [21]. Remarkably, a rather small j_c of about 4.5×10^{10} A m^{-2} is observed at $H_x = 300$ Oe in YIG(6 nm)/Pt(5 nm) with $H_K = 3.4$ kOe [22]. For the TbIG(5 nm)/Pt(5 nm) bilayer with $H_K \approx 1.5$ kOe, $j_c = 2.0 \times 10^{11}$ A m^{-2} at $H_x = 400$ Oe [23]. In addition to different individual layer thicknesses and different H_x magnitudes, quality fluctuation in the REIG heterostructures prepared under different experimental conditions may also lead to the invalidation of the correlation (if any) between j_c and PMA or the rare-earth-ion type of REIGs. In fact, the saturation magnetization (M_s) of YIG films with a relatively large threshold switching current is about 89 emu/cm^3 [21], which is appreciably lower than the YIG bulk value of 135 emu/cm^3, while the M_s of the TbIG films prepared for SOT switching is twice that of the TbIG bulk value [23]. It is theoretically predicted that the switching current is independent of the damping constant and is in almost linear relationship with H_K and H_x [24]. For the REIG–heavy-metal heterostructure, it is not clear how the threshold switching current varies with PMA magnitude or the rare-earth-ion type of REIGs.

Here, we investigate the perpendicular magnetic anisotropy of epitaxial $Y_{3-x}Tm_xFe_5O_{12}$ films over the full composition and comparatively characterize the magnetotransport properties and current-induced magnetization switching of the $Y_{3-x}Tm_xFe_5O_{12}$/Pt heterostructure with different Tm concentrations. A continuously tunable PMA is achieved with H_K varying from 0.3 to 2.7 kOe for 10-nm $Y_{3-x}Tm_xFe_5O_{12}$ by changing x from 0 to 3. The substituted films with x ranging from 0.6 to 1.2 are structurally much more robust against epitaxial strain relaxation. The heterostructure shows a significant anomalous Hall effect and spin Seebeck effect, and both change very little with Tm concentration, revealing the high-quality $Y_{3-x}Tm_xFe_5O_{12}$ surface and the dominant role of the net moment of Fe^{3+} sublattices in magnetotransport. Moreover, the SOT-induced switching is realized with a minor change in the threshold switching current, irrespective of the huge differences in perpendicular coercivity, H_c and H_K, at different Tm concentrations. The present study demonstrates that the Fe^{3+} sublattices dominate spin transfer in the REIG-Pt heterostructure, while the Tm^{3+} moments play a minor role, and the average spin-orbit coupling strength of RE^{3+} has no effect. In addition, the H_c- and H_K-insensitive switching currents for different REIGs will be of benefit for the development of insulating ferrimagnet spintronic devices.

II. EXPERIMENT

The substituted garnet $Y_{3-x}Tm_xFe_5O_{12}$ ($x = 0$, 0.6, 1.2, 1.8, 2.4, 3) films are prepared by cosputtering using commercially purchased $Y_3Fe_5O_{12}$ and $Tm_3Fe_5O_{12}$ targets. The films have thicknesses of 10 and 30 nm for each composition. The Y:Tm ratio is controlled by adjusting the sputtering power of the two targets. The Y, Tm, and Fe compositions in the films are checked by inductively coupled plasma atomic emission spectroscopy, which is consistent with the stoichiometry of $Y_{3-x}Tm_xFe_5O_{12}$ estimated by the sputtering rates of the two targets. The (111)-oriented $(Gd_{0.63}Y_{2.37})(Sc_2Ga_3)O_{12}$ (GYSGG) single-crystal substrates are deliberately treated prior to sputtering, and detailed information is published elsewhere [25]. The base pressure of the sputtering system is better than 4×10^{-6} Pa, and the working gas is high-purity Ar (99.999%) at 1.0 Pa. After deposition, all films are annealed at 800 °C for 2 h in a quartz tube with a pure oxygen pressure of 500 Pa under an oxygen flow rate of 45 sccm. Then the samples are rapidly cooled to room temperature by quickly moving the furnace away from the sample zone of the quartz tube to suppress strain relaxation. For magnetotransport measurements, a 3-nm Pt overlayer is sputter deposited on the annealed $Y_{3-x}Tm_xFe_5O_{12}$ films. After deposition, the whole films are patterned into a Hall bar shape with 20 μm width in both the channel and side bars by optical lithography and Ar^+-ion milling.

The crystalline structure and strain distribution of the $Y_{3-x}Tm_xFe_5O_{12}$ films are examined through x-ray diffraction (XRD) $2\theta/\omega$ scan and reciprocal space mapping (RSM) using Cu $K\alpha$ radiation on a Bruker AXS D8-Discover diffractometer. The surface morphology is measured by using an atomic force microscope (AFM). Magnetic properties are studied by vibrating-sample-magnetometer (VSM) and ferromagnetic resonance (FMR) results based on the vector-network-analyzer technique. During the FMR measurement, a static in-plane magnetic field up to 12 kOe is swept, while a microwave

magnetic field with a fixed frequency of 8–13 GHz is applied via a 100-μm-wide coplanar waveguide. The anomalous Hall effect (AHE) and longitudinal spin Seebeck effect (LSSE) for the $Y_{3-x}Tm_xFe_5O_{12}$/Pt stacks are investigated in the self-made magnetotransport measurement system. Details of the LSSE setup can be found elsewhere [26]. For current-induced switching measurements, a current pulse of a duration of 10 ms is applied along the longitudinal direction to excite SOT dynamics, and the response of the $Y_{3-x}Tm_xFe_5O_{12}$ magnetization is detected by the anamolous Hall effect after 1 s delay to eliminate the accumulated Joule heating effect. All measurements are performed on the annealed $Y_{3-x}Tm_xFe_5O_{12}$ films and the corresponding heterostructure at room temperature, unless otherwise specified.

III. RESULTS AND DISCUSSION

Epitaxial growth of the annealed $Y_{3-x}Tm_xFe_5O_{12}$ films and their epitaxial strains are investigated by XRD measurements. Figure 1(a) shows $2\theta/\omega$ scan spectra of the 10-nm $Y_{3-x}Tm_xFe_5O_{12}$ ($x = 0$, 0.6, 1.2, 1.8, 2.4, 3) films. In addition to the sharp (444) peak from the GYSGG substrate, the (444) diffraction peaks of the $Y_{3-x}Tm_xFe_5O_{12}$ films are identified without any peaks from impurity phases or other crystallographic orientations. Moreover, the film's (444) peaks progressively shift rightwards with x increasing. This is reasonable considering that the lattice constant of $Y_{3-x}Tm_xFe_5O_{12}$ decreases from 12.376 Å at $x = 0$ (for pure YIG) to 12.324 Å at $x = 3$ (for pure TmIG). It should also be pointed out that the $Y_{3-x}Tm_xFe_5O_{12}$ (444) plane spacing shrinks under a tensile strain provided by the GYSGG substrate with a larger lattice constant (12.507 Å), which will lead to a rightwards shift of the (444) peak in comparison with the case of strain-free bulk samples. From Fig. 1(a), one clearly observes a significant strain-induced peak shift for the pure YIG and TmIG films. The strain evolution for different samples is quantitated by the RSM measurement.

Figures 1(b)–1(e) show the RSM around the (486) diffraction peak for representative samples, including 10-nm-thick $Y_{3-x}Tm_xFe_5O_{12}$ ($x = 0.6$, 1.2, 1.8, and 3) and 30-nm-thick films with $x = 1.2$ and 3. First, we compare the results of 10-nm-thick films. The diffraction peaks for the $Y_{3-x}Tm_xFe_5O_{12}$ films with $x \leq 1.2$ are vertically aligned with the substrate peak, revealing that the films with Tm substitution up to $x = 1.2$ are fully strained to the GYSGG substrate. The further increase of Tm substitution leads to a slight deviation of the film diffraction peak with a larger $q_x(486)||[\bar{1}10]$, and there is an appreciable peak deviation or q_x increase for the TmIG film. Without doubt, partial relaxation of the epitaxial strain takes place in the 10-nm $Y_{3-x}Tm_xFe_5O_{12}$ films with $x \geq 1.8$ because of the too-large lattice mismatch. When the film thickness increases to 30 nm, $Y_{2.4}Tm_{0.6}Fe_5O_{12}$ and $Y_{1.8}Tm_{1.2}Fe_5O_{12}$

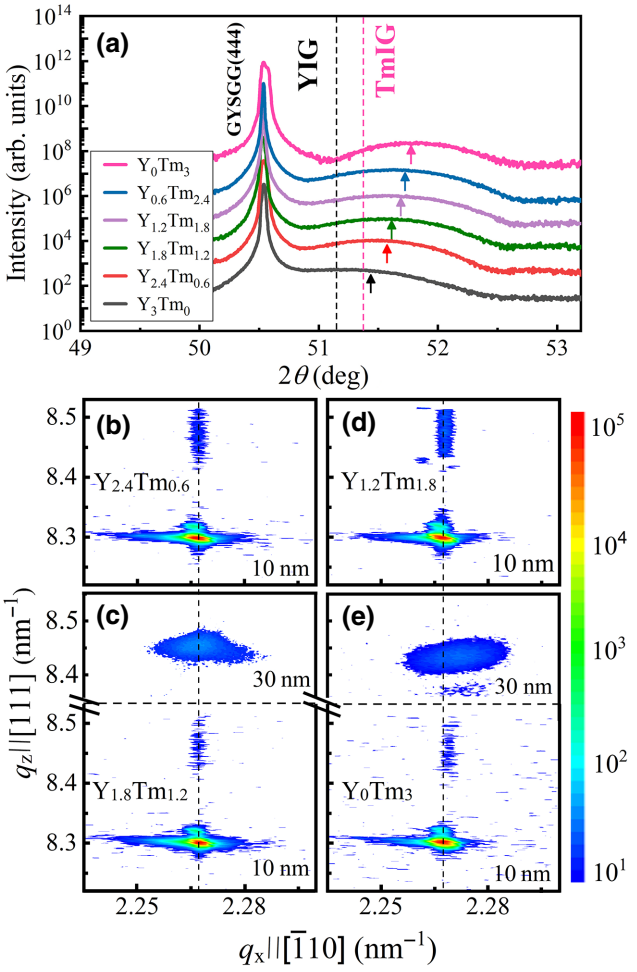

FIG. 1. (a) XRD $2\theta/\omega$ scan spectra of 10 nm $Y_{3-x}Tm_xFe_5O_{12}$ films on GYSGG substrates. Film peaks indicated with arrows shift rightwards with increasing Tm concentration. Vertical dashed lines are the positions of bulk YIG and TmIG. RSM of high-resolution XRD around (486) diffraction for (b) $Y_{2.4}Tm_{0.6}Fe_5O_{12}$ (10 nm), (c) $Y_{1.8}Tm_{1.2}Fe_5O_{12}$ (10 and 30 nm), (d) $Y_{1.2}Tm_{1.8}Fe_5O_{12}$ (10 nm), (e) $Tm_3Fe_5O_{12}$ (10 and 30 nm) film on GYSGG.

are still fully strained, but other films (including the 30-nm YIG film) exhibit partially relaxed epitaxial strains with increased peak q_x to reduce the too-large stress induced by the larger thickness. From Fig. 1(e), the 30-nm TmIG film apparently has a larger peak q_x in comparison with the 10-nm TmIG film. In contrast, 30-nm $Y_{1.8}Tm_{1.2}Fe_5O_{12}$ shown in Fig. 1(c) has almost the same peak q_x value as the 10-nm film, both identical to that of the substrate. From the $q_x(486)||[\bar{1}10]$ value, the (110)-plane spacing of the films is calculated using $d_{\text{film}}^{(110)} = (1/q_x) \times 2$, then the in-plane strain ($\varepsilon_{||}$)is estimated by $\varepsilon_{||} = [d_{\text{film}}^{(110)} - d_{\text{bulk}}^{(110)}]/d_{\text{bulk}}^{(110)}$. The peak q_x value and strain $\varepsilon_{||}$ of all $Y_{3-x}Tm_xFe_5O_{12}$ films are summarized in Table I, where the bulk lattice constants of the substituted garnets are assumed to be linearly varied with the Y:Tm composition. The theoretical strain,

TABLE I. The $q_x(486)||[\bar{1}10]$ and in-plane strain $\varepsilon_{||}$ of the 10- and 30-nm $Y_{3-x}Tm_xFe_5O_{12}$ films on (111)-oriented $(Gd_{0.63}Y_{2.37})(Sc_2Ga_3)O_{12}$ (GYSGG) single-crystal substrates. The corresponding q_x of the substrate is 2.261 nm^{-1}, and theoretical strain $\varepsilon_{||}$ for fully strained films are also given.

	q_x (nm^{-1})		$\varepsilon_{||}$ (%)		Theoretical $\varepsilon_{||}$ (%) under full strain
Composition	10 nm	30 nm	10 nm	30 nm	
Y_3Tm_0	2.261	2.263	1.05	0.98	1.05
$Y_{2.4}Tm_{0.6}$	2.261	2.261	1.15	1.15	1.15
$Y_{1.8}Tm_{1.2}$	2.261	2.261	1.24	1.24	1.24
$Y_{1.2}Tm_{1.8}$	2.265	2.267	1.14	1.08	1.31
$Y_{0.6}Tm_{2.4}$	2.267	2.268	1.15	1.12	1.39
Y_0Tm_3	2.269	2.271	1.15	1.00	1.48

$\varepsilon_{||}$, for ideally fully strained films are also included in Table I. The 10-nm YIG film has a full strain of $\varepsilon_{||} = 1.05\%$, but this strain is partially relaxed to $\varepsilon_{||} = 0.98\%$ when the YIG thickness increases to 30 nm. The substituted $Y_{3-x}Tm_xFe_5O_{12}$ ($x = 0.6$, 1.2) films show a larger full strain with a maximum of $\varepsilon_{||} = 1.24\%$ at $x = 1.2$, regardless of the film thickness. When $x \geq 1.8$, the strains for 10- and 30-nm films decrease to smaller values. The above results suggest that the substituted $Y_{3-x}Tm_xFe_5O_{12}$ films with x ranging from 0.6 to 1.2 are structurally much more robust against epitaxial strain relaxation. Finally, it should be pointed out that all $Y_{3-x}Tm_xFe_5O_{12}$ films have very smooth surfaces. The root-mean-square (rms) roughness of the 10-nm films is below 0.4 nm over a scanning area $5 \times 5\ \mu m^2$ from the AFM observation, indicating the atomically flat surface.

As is known, TmIG has a relatively large negative magnetostriction constant with $\lambda_{111} = -5.2 \times 10^{-6}$, which is larger than twice the corresponding value of YIG (-2.4×10^{-6}). One can expect that substituted $Y_{3-x}Tm_xFe_5O_{12}$ has a negative λ_{111} with its magnitude increasing with an increase of the Tm concentration. With PMA demonstrated in thin YIG films on (111) GYSGG through magnetoelastic anisotropy previously [18], the thin substituted $Y_{3-x}Tm_xFe_5O_{12}$ films on (111) GYSGG should present a larger PMA. We measure M-H loops of all samples with a field applied along the in-plane and out-of-plane directions. Figures 2(a)–2(f) show the normalized hysteresis loops of the 10-nm $Y_{3-x}Tm_xFe_5O_{12}$ films with paramagnetic substrate signals removed. PMA is evident for all $Y_{3-x}Tm_xFe_5O_{12}$ ($0 \leq x \leq 3$) films, judging from the square perpendicular M-H loops and rather slanted in-plane M-H curves. One can further note that the perpendicular coercivity (H_c) monotonically increases from 2 Oe for the pure YIG film ($x = 0$) to about 65 Oe for pure TmIG ($x = 3$), and the effective PMA field, H_K, corresponding to the saturation field of the in-plane magnetization curve, consistently increases from 0.3 to 2.7 kOe. The perpendicular H_c and H_K of different samples are summarized in Fig. 2(g). Both increase with Tm concentration, but it seems that the increasing tendency of H_K at $x > 1.8$ slows down, to some extent, possibly due to the partial relaxation of epitaxial strain for these films. For the 30-nm-thick films, the YIG film ($x = 0$) no longer exhibits PMA, whereas other $Y_{3-x}Tm_xFe_5O_{12}$ films possess PMA with H_K of about 1.6–1.7 kOe at $1.2 \leq x \leq 3$. The magnetoelastic anisotropy of YIG and Tm-rich $Y_{3-x}Tm_xFe_5O_{12}$ films is appreciably reduced at large thicknesses because of the partial relaxation of strain. Remarkably, the films of $Y_{2.4}Tm_{0.6}Fe_5O_{12}$ and $Y_{1.8}Tm_{1.2}Fe_5O_{12}$, regardless of the thickness, have a robust H_K of about 1.2 and 1.6 kOe, respectively. Magnetically, it is consistent with effective suppression of strain relaxation in the 30-nm $Y_{3-x}Tm_xFe_5O_{12}$ films with $x = 0.6$ and 1.2. Finally, the saturation magnetization ($4\pi M_s$) of $Y_{3-x}Tm_xFe_5O_{12}$ films is extracted from the M-H measurements, and the corresponding results are presented in Fig. 2(h). Note that $4\pi M_s$ monotonically decreases from 1680 to 1300 Gs as the Tm concentration increases from $x = 0$ to $x = 3$, roughly consistent with bulk YIG and TmIG values [1,27].

To study the dynamic magnetic properties of $Y_{3-x}Tm_xFe_5O_{12}$ films, FMR spectra at different frequencies are measured with an in-plane field. Figure 3 shows the typical FMR results of three representative samples, 10-nm-thick YIG, $Y_{1.8}Tm_{1.2}Fe_5O_{12}$, and TmIG. From spectral fitting (see the insets of Fig. 3), the resonance field (H_{res}) and linewidth (ΔH) are extracted at each frequency (f). Based on the frequency dependence of H_{res} displayed in Figs. 3(a), 3(c), and 3(e), the effective PMA field of the three samples is determined by using the Kittel equation:

$$f = |\gamma|\sqrt{H_{res}(H_{res} - H_K)},$$

where $|\gamma|$ is the absolute gyromagnetic ratio. H_K is about 0.33 kOe for YIG, 1.97 kOe for $Y_{1.8}Tm_{1.2}Fe_5O_{12}$, and 2.56 kOe for TmIG. These values are consistent with those obtained from VSM measurements. As for the linewidth, it varies linearly with resonance frequency, as shown in Figs. 3(b), 3(d), and 3(f). The Gilbert damping constant, α, is thus determined through the expression

$$\Delta H = \frac{2\alpha}{|\gamma|} f + \Delta H_0,$$

where ΔH_0 accounts for inhomogeneous linewidth broadening. The α value shows a monotonic increase from $(7.3 \pm 0.1) \times 10^{-4}$ for YIG to 0.023 ± 0.002 for $Y_{1.8}Tm_{1.2}IG$, eventually to 0.033 ± 0.004 for TmIG. This is expected because rare-earth ions, such as Tm^{3+}, are known to relax rapidly compared with the Fe ions [28]. The Gilbert damping constants for the present YIG and TmIG films with PMA are comparable to those reported

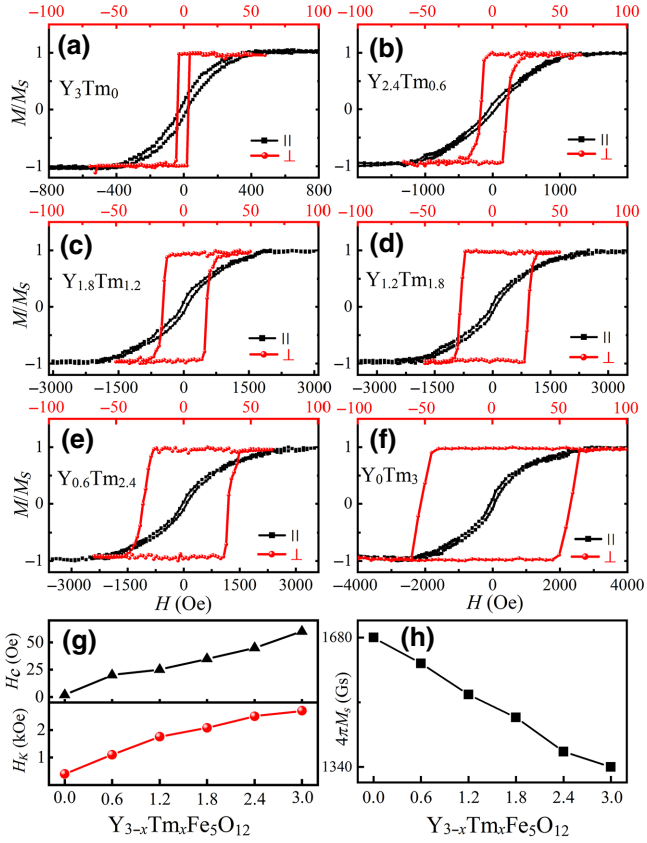

FIG. 2. Perpendicular (top x axis) and in-plane (bottom x axis) M-H curves of the 10-nm $Y_{3-x}Tm_xFe_5O_{12}$ films on (111) GYSGG substrates with (a) $x=0$, (b) $x=0.6$, (c) $x=1.2$, (d) $x=1.8$, (e) $x=2.4$, and (f) $x=3$. Dependence of (g) H_c and H_K and (h) $4\pi M_s$ on Tm concentration for the 10-nm $Y_{3-x}Tm_xFe_5O_{12}$ films.

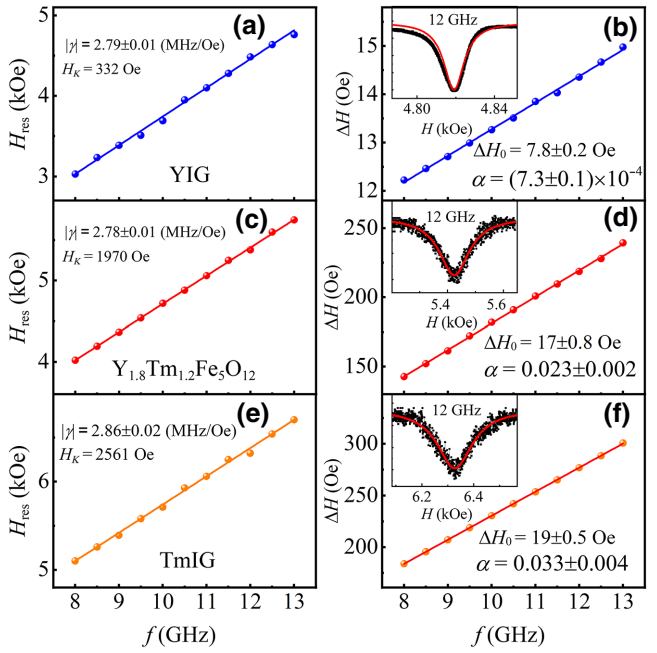

FIG. 3. Frequency dependence of resonance field for 10-nm-thick (a) YIG, (c) $Y_{1.8}Tm_{1.2}Fe_5O_{12}$, (e) TmIG, and variation of linewidth as a function of frequency for 10-nm-thick (b) YIG, (d) $Y_{1.8}Tm_{1.2}Fe_5O_{12}$, (f) TmIG. Insets show corresponding FMR spectra at 12 GHz.

before: $\alpha = 4.2 \times 10^{-4}$ for YIG [22] and 0.011 for TmIG [29]. The gradual increase of α with Tm concentration suggests that a relatively low damping with significant PMA can be achieved in the rare-earth-ion-substituted YIG films. It should be parenthetically mentioned that the fitted inhomogeneous ΔH_0 is 7.8 ± 0.2, 17 ± 0.8, and 19 ± 0.5 Oe for YIG, $Y_{1.8}Tm_{1.2}Fe_5O_{12}$, and TmIG, respectively. As is known, line broadening, ΔH_0, due to inhomogeneities arises from the simple superposition of the shifted local FMR profiles at different regions because of the fluctuation of the magnetic properties. For the present $Y_{3-x}Tm_xFe_5O_{12}$ films, different lattice mismatches between the film and substrate may lead to different amounts of defects and oxygen vacancies, and different magnitudes of local strains, thus giving rise to different ΔH_0.

We measure the LSSE and AHE of the patterned $Y_{3-x}Tm_xFe_5O_{12}$(10 nm)/Pt(3 nm) stacks over the full composition to further study the perpendicular magnetic properties, particularly the substituted-garnet-surface magnetism and the exchange interaction across the heterostructured interface. Figure 4(a) shows the in-plane field dependence of the thermal voltages of the samples within the LSSE configuration near room temperature. For the REIG-Pt heterostructure, the observed thermal voltage mostly stems from the LSSE [30], possibly together with some contribution of the anomalous Nernst effect (ANE) due to the magnetic proximity effect (MPE) of Pt [31]. The LSSE voltage is proportional to the in-plane magnetization component along the field direction, so is the ANE signal, if there is one. The saturation fields of the slanted thermal voltage loops thus represent the H_K of the perpendicularly magnetized $Y_{3-x}Tm_xFe_5O_{12}$ layers. Figure 4(b) shows the room-temperature AHE resistance of all samples as a function of the perpendicular field with ordinary Hall effect signals subtracted. With AHE being proportional to the perpendicular magnetization component, the square AHE loops reconfirm the PMA of the 10-nm $Y_{3-x}Tm_xFe_5O_{12}$ layers. From Figs. 4(a) and 4(b), it is clear that perpendicular H_c and H_K derived from the magnetotransport measurements increase appreciably with the Tm concentration; this is consistent with those values obtained from the M-H curves of the single-layer films. However, one could find that there is some difference in H_c between the AHE and perpendicular M-H loops, and the H_K value determined from the thermal voltage loops is overall a little

bit smaller. This seems to be caused by sample patterning and/or PMA modification upon deposition of the Pt overlayer [29]. It is noteworthy that the magnitude of the LSSE or ANE voltage remains nearly unchanged for different samples, although perpendicular H_c, H_K, and $4\pi M_s$ vary considerably with the Tm concentration. The saturated AHE resistance seems to show, more or less, some variation for samples with different Tm concentrations. To clarify the role of REIG magnetization in the AHE, the Hall loops of all $Y_{3-x}Tm_xFe_5O_{12}$(10 nm)/Pt(3 nm) samples are measured at low temperatures. Square AHE loops are still observed at temperatures down to 50 K for all these films. The saturated AHE resistance (R^s_{AHE}) of the six samples at different temperatures is summarized in Fig. 3(c). Note that the negative R^s_{AHE} with slightly different magnitudes for different samples monotonically increases to positive values at similar rates as the temperature decreases from 300 to 50 K. It should be emphasized that the saturation magnetization varies in opposite directions for YIG and TmIG when the temperature is below 200 K. In fact, the $4\pi M_s$ of YIG, about 26% larger than that of TmIG at 300 K, becomes about 3 times as large as that of TmIG at 50 K [1]. Therefore, it is very likely that the R^s_{AHE} of the heterostructure has a weak, if any, correlation with the $4\pi M_s$ of the $Y_{3-x}Tm_xFe_5O_{12}$ layer, and the observed difference in R^s_{AHE} among samples at different temperatures might be attributed to sample fluctuation, most probably the sample-surface magnetism fluctuation.

The LSSE in the REIG-Pt heterostructure refers to the thermal-gradient-induced spin currents being transmitted to Pt and further converted into a transverse charge current, here the spin-current transmission is realized via the interface *s-d* exchange interaction in terms of the spin-mixing conductance. As for the AHE in the REIG-Pt heterostructure, it is believed to have two contributions. One originates from the nonequilibrium spin Hall effect through the imaginary part of the spin-mixing conductance, denoted as SH AHE [32]; the other stems from the MPE of Pt because of the direct *d-d* exchange interaction between the interfacial Fe^{3+} ions and Pt atoms, denoted as MPE AHE [31, 33,34]. Depending on the interface, MPE could be either dominant or negligible. The sign change of R^s_{AHE} at different temperatures suggests that both MPE AHE and SH AHE with opposite signs are present in our samples, and the MPE contribution to AHE becomes dominant when the temperature is lowered; this was demonstrated previously [35]. Two points can be drawn from the AHE and LSSE results. First, the net magnetic moment of Fe^{3+} sublattices, rather than the total magnetic moment of $Y_{3-x}Tm_xFe_5O_{12}$, is predominant for magnetotransport across the interface. Second, the interface spin-current transmission and interface spin-exchange interaction are barely influenced by the Tm concentration. Finally, we would like to point out that the value of the room-temperature AHE resistivity for the $Y_{3-x}Tm_xFe_5O_{12}$(10 nm)/Pt(3 nm) bilayers is

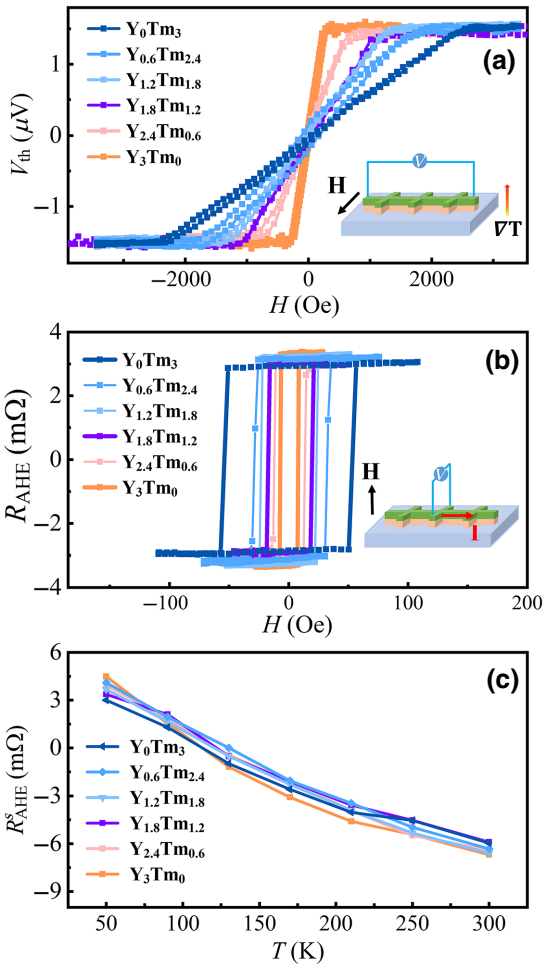

FIG. 4. (a) In-plane field dependence of thermal voltage, (b) perpendicular field dependence of anomalous Hall resistance, and (c) temperature-dependent R_{AHE} for $Y_{3-x}Tm_xFe_5O_{12}$(10 nm)/Pt (3 nm) stacks. Insets in (a),(b) are respective schematic diagrams of the measurements.

calculated to be about 1.4 nΩ cm. It is comparable to that for PLD epitaxial YIG/Pt stacks with in-plane anisotropy [36], reflecting the highly qualified surface magnetism of the current $Y_{3-x}Tm_xFe_5O_{12}$ films with PMA.

Now we explore current-induced switching for the $Y_{3-x}Tm_xFe_5O_{12}$(10 nm)/Pt(3 nm) devices with different compositions. Detailed results of three representative samples, YIG/Pt, $Y_{1.8}Tm_{1.2}Fe_5O_{12}$/Pt, and TIG/Pt, are summarized in Fig. 5. With AHE resistance references for up (down) magnetization alignments established in the Hall measurements [see Fig. 4(b)], information about the perpendicular magnetization state after applying switching-current pulses (1–15 mA) is acquired by measuring the corresponding AHE resistance through a pair of plus (minus) sensing-current pulses (0.2 mA). The width of switching and sensing pulses is 10 ms. An in-plane field (H_x) of ±10 Oe is applied along the current direction

(x axis) to break the rotational symmetry of the spin-orbit torque, τ_{SOT}, and lead to deterministic switching. Figure 5(a) shows the magnetization switching behavior of YIG/Pt as a function of current density (j) at $H_x = 10$ Oe; here the measured AHE resistance, R_{AHE}, is normalized by the saturated AHE resistance, R^s_{AHE}, for AHE loop measurements. Note that the switching events systematically approach reversal above the threshold current density, $j_t = 1.43 \times 10^{11}$ A m^{-2}, where about 50% of the Hall cross region is reversed, until complete switching is realized at a critical current density of $j_c = 1.76 \times 10^{11}$ A m^{-2}. Above j_c, the magnetization switches systematically and reproducibly. In Fig. 5(b), we show the measured Hall resistance in response to a series of plus and minus switching pulses at a density of 1.76×10^{11} A m^{-2}. R_{AHE} changes by 100% with respect to its full amplitude of about 3.2 mΩ. The switching polarity reverses when reversing the in-plane field from $H_x = 10$ to -10 Oe, as expected from the SOT-induced switching. The critical current density, j_c, at $H_x = 10$ Oe for the present YIG(10 nm)/Pt(3 nm) stack is somewhat smaller than the corresponding value of 3×10^{11} A m^{-2} at a much higher $H_x = 50$ Oe obtained previously in YIG(5 nm)/Pt(3 nm) [21]. We would like to point out that these earlier reported perpendicular YIG films for SOT switching exhibit a lower saturation magnetization than the bulk value. The present results indicate that interfacial spin transmission in our YIG/Pt bilayer is very efficient due to the high-quality $Y_{3-x}Tm_xFe_5O_{12}$ layers. The SOT switching curves of the $Y_{1.8}Tm_{1.2}Fe_5O_{12}(10)/Pt(3)$ and TmIG(10)/Pt(3) stacks are detailed in Figs. 5(c)–5(f). There are only tiny increments for the threshold and critical current densities in the presence of more and more Tm ions, i.e., for $Y_{1.8}Tm_{1.2}Fe_5O_{12}$/Pt, $j_t = 1.50 \times 10^{11}$ A m^{-2} and $j_c = 1.80 \times 10^{11}$ A m^{-2}; for TmIG/Pt, $j_t = 1.53 \times 10^{11}$ A m^{-2} and $j_c = 1.83 \times 10^{11}$ A m^{-2}, all at $H_x = 10$ Oe. The critical current density of the present TmIG/Pt stack is almost equal to the value reported in the PLD epitaxial TmIG(9.6 nm)/Pt(4 nm) stack [5,20], reconfirming the efficient interfacial spin transmission of the sputter-prepared heterostructure. It should be emphasized that the perpendicular H_c and H_K for the $Y_{3-x}Tm_xFe_5O_{12}$/Pt stacks enormously increase with Tm concentration. From Fig. 4, one notes $H_c = 8$ Oe, $H_K = 300$ Oe for YIG/Pt; $H_c = 25$ Oe, $H_K = 1700$ Oe for $Y_{1.8}Tm_{1.2}Fe_5O_{12}$/Pt; and $H_c = 55$ Oe, $H_K = 2300$ Oe for TmIG/Pt. This is in striking contrast to the minor changes in threshold and critical current density for the corresponding samples. One expects that the critical current will increase substantially with Tm concentration, in accordance with the greatly enhanced H_K, based on the simplified analytical expression of the SOT switching current due to the spin Hall effect (SHE) [24]:

$$j_c = \frac{2e}{\hbar}\frac{M_s t_F}{\theta_{SH}}\left(\frac{H_K}{2} - \frac{H_x}{\sqrt{2}}\right),$$

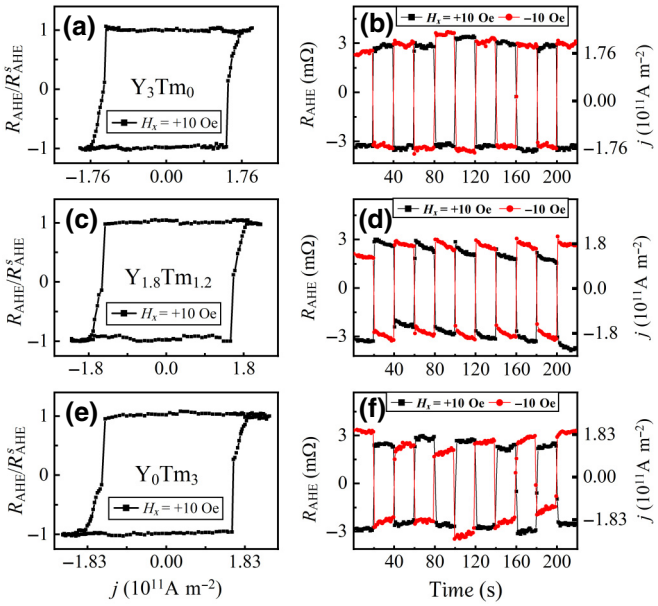

FIG. 5. Normalized AHE resistance as a function of current density in a given in-plane field of $H_x = 10$ Oe for (a) YIG/Pt, (c) $Y_{1.8}Tm_{1.2}Fe_5O_{12}$/Pt, and (e) TmIG/Pt. AHE resistance in response to a series of plus (minus) switching pulses for (b) YIG/Pt at a current density of 1.76×10^{11} A m^{-2}, (d) $Y_{1.8}Tm_{1.2}Fe_5O_{12}$/Pt at a current density of 1.80×10^{11} A m^{-2}, (f) TmIG/Pt at a current density of 1.80×10^{11} A m^{-2} in the presence of field $H_x = \pm 10$ Oe. Insulating ferromagnetic layer thickness is 10 nm, and Pt layer is 3 nm thick.

where t_F is the thickness of the ferromagnetic layer; θ_{SH} is an effective spin Hall angle of Pt.

Magnetization reversal in insulating ferromagnet-Pt heterostructures driven by SOT shares the same mechanisms as those driven by a magnetic field, i.e., reverse domain nucleation, domain-wall depinning, and propagation. As is known, domains are usually pinned at defect and dislocations sites. Compared with magnetization reversal by the field, the deterministic step of current-induced reversal is thermally assisted depinning under the influence of a SHE-induced equivalent field [37]. Current flowing in the Pt layer may have a dynamic effect on defects, e.g., weakening the defect-pinning effects on domains. Charge-current-induced Joule heating will also contribute to the depinning of domains, which further averages the depinning effects for all $Y_{3-x}Tm_xFe_5O_{12}$ films. On the other hand, current-induced switching is strongly influenced by spin transport at the interface, which is irrespective of the strength of PMA. The results of the AHE and LSSE prove that the $Y_{3-x}Tm_xFe_5O_{12}$/Pt stacks with different PMA possess similar or identical spin-transport efficiencies. To some extent, H_K-insensitive switching current in $Y_{3-x}Tm_xFe_5O_{12}$/Pt devices can be determined by many factors. To clarify this issue, more in-depth work is needed in the future. From the SOT results

of $Y_{3-x}Tm_xFe_5O_{12}$/Pt, one can conclude that the Fe^{3+} sublattice spins dominate spin transfer, while the Tm^{3+} moments play a minor role, and the average spin-orbit coupling strength of RE^{3+} plays no part. In addition, the almost constant critical current density, irrespective of the magnitude of H_K for Tm-substituted YIG at any composition, will be of benefit to insulating spintronic device development. Finally, we would like to point out that magnetization-compensated ferrimagnets [e.g., Co-Gd, (Gd, Fe)Co alloys] are reported to exhibit significant SOT enhancement around the magnetic compensation temperature [38] or around the angular-moment compensation temperature [39]. Considering that REIGs have multiple antiferromagnetic coupled sublattices and different magnetic compensation temperatures for some rare-earth ions, it is worth further exploring various REIGs, including rare-earth-ion-substituted REIG films, to reduce the switching current at room temperature.

IV. CONCLUSION

We obtain a large tunable PMA in 10-nm $Y_{3-x}Tm_xFe_5O_{12}$ films with effective PMA fields, H_K, ranging from 0.3 to 2.7 kOe by changing the Tm concentration. The substituted $Y_{3-x}Tm_xFe_5O_{12}$ films with x ranging from 0.6 to 1.2 are structurally much more robust against epitaxial strain relaxation. The heterostructure of $Y_{3-x}Tm_xFe_5O_{12}$/Pt shows an appreciable AHE signal and LSSE voltage, and both of them change little with Tm composition, revealing the high-quality $Y_{3-x}Tm_xFe_5O_{12}$ surface with nearly identical spin-current transmission and exchange interactions across the heterostructured interface. More importantly, we further demonstrate efficient SOT-induced magnetization switching in the $Y_{3-x}Tm_xFe_5O_{12}$/Pt stacks and find that the critical current density is almost independent of the effective PMA field. Our results demonstrate that substituted rare-earth iron garnets can be a general approach to tune PMA within a large range with nearly unchanged switching currents, and yet there is plenty of work left to be done for more efficient SOT-based REIG spintronics devices.

ACKNOWLEDGMENTS

The authors thank Ms. Shuyao Chen and Professor Tao Liu of the School of Electronic Science and Engineering, University of Electronic Science and Technology of China for the FMR measurements. This work is supported by the National key R&D plan program of China (Grant No. 2016YFA0300804), the National Natural Science Foundation of China (Grant No. 51871236) and the China Postdoctoral Science Foundation (Grant No. DG211I4A1A).

[1] A. Paoletti, *Physics of magnetic garnets* (North-Holland Publishing Company, Amsterdam, 1978).
[2] S. A. Manuilov, S. I. Khartsev, and A. M. Grishin, Pulsed laser deposited $Y_3Fe_5O_{12}$ films: Nature of magnetic anisotropy I, J. Appl. Phys **106**, 123917 (2009).
[3] P. Paroli, Magneto-optical devices based on garnet films, Thin Solid Films **114**, 187 (1984).
[4] O. Kamada, T. Nakaya, and S. Higuchi, Magnetic field optical sensors using Ce:YIG single crystals as a Faraday element, Sens. Actuators, A **119**, 345 (2005).
[5] C. O. Avci, A. Quindeau, C. F. Pai, M. Mann, L. Caretta, A. S. Tang, M. C. Onbasli, C. A. Ross, and G. S. Beach, Current-induced switching in a magnetic insulator, Nat. Mater **16**, 309 (2017).
[6] J. J. Bauer, E. R. Rosenberg, S. Kundu, K. A. Mkhoyan, P. Quarterman, A. J. Grutter, B. J. Kirby, J. A. Borchers, and C. A. Ross, Dysprosium iron garnet thin films with perpendicular magnetic anisotropy on silicon, Adv. Electron. Mater. **6**, 1900820 (2020).
[7] J. Wunderlich, Spintronics: Current-switched magnetic insulator, Nat. Mater. **16**, 284 (2017).
[8] A. Rosencwaig and W. J. Tabor, Noncubic garnet anisotropy from growth-induced pair ordering, J. Appl. Phys. **42**, 1643 (1971).
[9] J. J. Bauer, E. R. Rosenberg, and C. A. Ross, Perpendicular magnetic anisotropy and spin mixing conductance in polycrystalline europium iron garnet thin films, Appl. Phys. Lett. **114**, 052403 (2019).
[10] M. Kubota, A. Tsukazaki, F. Kagawa, K. Shibuya, Y. Tokunaga, M. Kawasaki, and Y. Tokura, Stress-induced perpendicular magnetization in epitaxial iron garnet thin films, Appl. Phys. Exp. **5**, 103002 (2012).
[11] G. Vilela, H. Chi, G. Stephen, C. Settens, P. Zhou, Y. Ou, D. Suri, D. Heiman, and J. S. Moodera, Strain-tuned magnetic anisotropy in sputtered thulium iron garnet ultrathin films and TIG/Au/TIG valve structures, J. Appl. Phys. **127**, 115302 (2020).
[12] M. Kubota, K. Shibuya, Y. Tokunaga, F. Kagawa, A. Tsukazaki, Y. Tokura, and M. Kawasaki, Systematic control of stress-induced anisotropy in pseudomorphic iron garnet thin films, J. Magn. Magn. Mater. **339**, 63 (2013).
[13] V. H. Ortiz, M. Aldosary, J. Li, Y. Xu, M. I. Lohmann, P. Sellappan, Y. Kodera, J. E. Garay, and J. Shi, Systematic control of strain-induced perpendicular magnetic anisotropy in epitaxial europium and terbium iron garnet thin films, APL Mater. **6**, 121113 (2018).
[14] E. R. Rosenberg, L. Beran, C. O. Avci, C. Zeledon, B. Song, F. C. Gonzalez, J. Mendil, P. Gambardella, M. Veis, C. Garcia, G. S. D. Beach, and C. A. Ross, Magnetism and spin transport in rare-earth-rich epitaxial terbium and europium iron garnet films, Phys. Rev. Mater. **2**, 094405 (2018).
[15] C. T. Wang, X. F. Liang, Y. Zhang, X. Liang, Y. P. Zhu, J. Qin, Y. Gao, B. Peng, N. X. Sun, and L. Bi, Controlling the magnetic anisotropy in epitaxial $Y_3Fe_5O_{12}$ films by manganese doping, Phys. Rev. B **96**, 224403 (2017).
[16] A. Kehlberger, K. Richter, M. C. Onbasli, G. Jakob, D. H. Kim, T. Goto, C. A. Ross, G. Götz, G. Reiss, T. Kuschel, and M. Kläui, Enhanced Magneto-Optic Kerr Effect and Magnetic Properties of $CeY_2Fe_5O_{12}$ Epitaxial Thin Films, Phys. Rev. Appl. **4**, 014008 (2015).

[17] L. Soumah, N. Beaulieu, L. Qassym, C. Carretero, E. Jacquet, R. Lebourgeois, J. B. Youssef, P. Bortolotti, V. Cros, and A. Anane, Ultra-low damping insulating magnetic thin films get perpendicular, Nat. Commun. **9**, 3355 (2018).

[18] G. Li, H. Bai, J. Su, Z. Z. Zhu, Y. Zhang, and J. W. Cai, Tunable perpendicular magnetic anisotropy in epitaxial $Y_3Fe_5O_{12}$ films, APL Mater. **7**, 041104 (2019).

[19] J. Fu, M. Hua, X. Wen, M. Xue, S. Ding, M. Wang, P. Yu, S. Liu, J. Han, C. Wang, H. Du, Y. Yang, and J. Yang, Epitaxial growth of $Y_3Fe_5O_{12}$ thin films with perpendicular magnetic anisotropy, Appl. Phys. Lett. **110**, 202403 (2017).

[20] C. O. Avci, E. Rosenberg, M. Baumgartner, L. Beran, A. Quindeau, P. Gambardella, C. A. Ross, and G. S. D. Beach, Fast switching and signature of efficient domain wall motion driven by spin-orbit torques in a perpendicular anisotropy magnetic insulator/Pt bilayer, Appl. Phys. Lett. **111**, 072406 (2017).

[21] C. Y. Guo, C. H. Wan, M. K. Zhao, H. Wu, C. Fang, Z. R. Yan, J. F. Feng, H. F. Liu, and X. F. Han, Spin-orbit torque switching in perpendicular $Y_3Fe_5O_{12}$/Pt bilayer, Appl. Phys. Lett. **114**, 192409 (2019).

[22] J. Ding, C. Liu, Y. Zhang, U. Erugu, Z. Quan, R. Yu, E. McCollum, S. Mo, S. Yang, H. F. Ding, X. Xu, J. Tang, X. Yang, and M. Wu, Nanometer-Thick Yttrium Iron Garnet Films with Perpendicular Anisotropy and Low Damping, Phys. Rev. Appl. **14**, 014017 (2020).

[23] H. Chen, D. Cheng, H. Yang, D. Wang, S. Zhou, Z. Shi, and X. Qiu, Magnetization switching induced by magnetic field and electric current in perpendicular TbIG/Pt bilayers, Appl. Phys. Lett. **116**, 112401 (2020).

[24] K. S. Lee, S. W. Lee, B. C. Min, and K. J. Lee, Threshold current for switching of a perpendicular magnetic layer induced by spin Hall effect, Appl. Phys. Lett. **102**, 112410 (2013).

[25] H. Bai, X. Z. Zhan, G. Li, J. Su, Z. Z. Zhu, Y. Zhang, T. Zhu, and J. W. Cai, Characterization of YIG thin films and vacuum annealing effect by polarized neutron reflectometry and magnetotransport measurements, Appl. Phys. Lett. **115**, 182401 (2019).

[26] X. L. Zheng, L. K. Zou, Y. Zhang, and J. W. Cai, Large Inverse Spin Hall Effect in Co-Pt Spin-Valve Heterostructures, Phys. Rev. Appl. **7**, 044003 (2017).

[27] T. Yamagishi, J. Awaka, Y. Kawashima, M. Uemura, S. Ebisu, S. Chikazawa, and S. Nagata, Ferrimagnetic order in the mixed garnet $(Y_{1-x}Gd_x)_3Fe_5O_{12}$, Philos. Mag. **85**, 1819 (2005).

[28] C. Kittel, Theory of ferromagnetic resonance in rare earth garnets, Phys. Rev. **115**, 1587 (1959).

[29] A. J. Lee, A. S. Ahmed, B. A. McCullian, S. Guo, M. Zhu, S. Yu, P. M. Woodward, J. Hwang, P. C. Hammel,and F. Yang, Interfacial Rashba-Effect-Induced Anisotropy in Nonmagnetic-Material–Ferrimagnetic-Insulator Bilayers, Phys. Rev. Lett. **124**, 257202 (2020).

[30] T. Kikkawa, K. Uchida, Y. Shiomi, Z. Qiu, D. Hou, D. Tian, H. Nakayama, X. F. Jin, and E. Saitoh, Longitudinal Spin Seebeck Effect Free from the Proximity Nernst Effect, Phys. Rev. Lett. **110**, 067207 (2013).

[31] Y. M. Lu, Y. Choi, C. M. Ortega, X. M. Cheng, J. W. Cai, S. Y. Huang, L. Sun, and C. L. Chien, Pt Magnetic Polarization on $Y_3Fe_5O_{12}$ and Magnetotransport Characteristics, Phys. Rev. Lett. **110**, 147207 (2013).

[32] H. Nakayama, M. Althammer, Y. T. Chen, K. Uchida, Y. Kajiwara, D. Kikuchi, T. Ohtani, S. Geprags, M. Opel, S. Takahashi, R. Gross, G. E. Bauer, S. T. Goennenwein, and E. Saitoh, Spin Hall Magnetoresistance Induced by a Nonequilibrium Proximity Effect, Phys. Rev. Lett. **110**, 206601 (2013).

[33] C. Tang, P. Sellappan, Y. Liu, Y. Xu, J. E. Garay, and J. Shi, Anomalous Hall hysteresis in $Tm_3Fe_5O_{12}$/Pt with strain-induced perpendicular magnetic anisotropy, Phys. Rev. B **94**, 140403(R) (2016).

[34] X. Liang, Y. Zhu, B. Peng, L. Deng, J. Xie, H. Lu, M. Wu, and L. Bi, Influence of interface structure on magnetic proximity effect in Pt/$Y_3Fe_5O_{12}$ heterostructures, ACS Appl. Mater. Interfaces **8**, 8175 (2016).

[35] Q. Shao, A. Grutter, Y. Liu, G. Yu, C. Y. Yang, D. A. Gilbert, E. Arenholz, P. Shafer, X. Che, C. Tang, M. Aldosary, A. Navabi, Q. L. He, B. J. Kirby, J. Shi, and K. L. Wang, Exploring interfacial exchange coupling and sublattice effect in heavy metal/ferrimagnetic insulator heterostructures using Hall measurements, x-ray magnetic circular dichroism, and neutron reflectometry, Phys. Rev. B **99**, 104401 (2019).

[36] S. Meyer, R. Schlitz, S. Geprägs, M. Opel, H. Huebl, R. Gross, and S. T. B. Goennenwein, Anomalous Hall effect in YIG/Pt bilayers, Appl. Phys. Lett. **106**, 132402 (2015).

[37] Z. Ren, K. Qian, M. Aldosary, Y. Liu, S. K. Cheung, I. Ng, J. Shi, and Q. Shao, Strongly heat-assisted spin–orbit torque switching of a ferrimagnetic insulator, APL Mater. **9**, 051117 (2021).

[38] R. Mishra, J. Yu, X. Qiu, M. Motapothula, T. Venkatesan, and H. Yang, Anomalous Current-Induced Spin Torques in Ferrimagnets near Compensation, Phys. Rev. Lett. **118**, 167201 (2017).

[39] Y. Hirata, D. H. Kim, T. Okuno, T. Nishimura, D. Y. Kim, Y. Futakawa, H. Yoshikawa, A. Tsukamoto, K. J. Kim, S. B. Choe, and T. Ono, Correlation between compensation temperatures of magnetization and angular momentum in GdFeCo ferrimagnets, Phys. Rev. B **97**, 220403(R) (2018).